

Discovery of optical emission from the supernova remnant G108.2–0.6 and its atomic environment

G. Paylı¹★, H. Bakış¹†, E. Aktekin², H. Sano³, and A. Sezer⁴

¹Department of Space Sciences and Technologies, Akdeniz University, 07058, Antalya, Turkey

²Department of Physics, Süleyman Demirel University, 32000, Isparta, Turkey

³Faculty of Engineering, Gifu University, 1-1 Yanagido, Gifu 501-1193, Japan

⁴Department of Computer Engineering, Avrasya University, 61250, Trabzon, Turkey

Accepted XXX. Received YYY; in original form ZZZ

ABSTRACT

We report the first detection of optical emission from the shell-type Galactic supernova remnant (SNR) G108.2–0.6. We obtained H α images and long-slit spectra using the 1.5-m RTT150 telescope to examine the morphological and spectral characteristics of the SNR. We detected several filaments along its north and south regions, which is consistent with its SNR nature. The spectra exhibit [S II]/H α ratios in the range of 0.4–1.1, indicating emission from shock-heated gas. The oxygen doublet emission lines [O I] λ 6300, λ 6363 detected in the south region also support the indicator of the presence of shocks. We estimate the electron density using the [S II] 6716/6731 ratio ranging from 15 to 1800 cm⁻³. The spectra show a relatively low shock velocity of $V_s \sim 80$ km s⁻¹ with the pre-shock cloud density of $n_c \sim 18$ –57 cm⁻³. The H α /H β ratios show significant variation across the observed regions with extinction $E(B - V)$ ranging from 0.22 to 1.65. We also analyzed the archival H I data and estimated the kinematic distance to the SNR of ~ 0.8 kpc and dynamical age as $\sim 70 \pm 10$ kyr of G108.2–0.6.

Key words: ISM: individual objects: G108.2–0.6 – ISM: supernova remnants – H II regions – atomic data

1 INTRODUCTION

Supernova remnants (SNRs) provide us with important information on the supernova explosion mechanism, properties of the surrounding medium, and their interaction (see Vink 2020, for a review). Most SNRs have been detected in radio wavelengths due to their nonthermal synchrotron emission (e.g. Dubner & Giacani 2015; Green 2019). Optical observations of SNRs allow us to inspect the SNR properties such as the morphology, the properties of the shocked gas, and the density of the ambient medium (e.g. Stupar, Parker & Filipovic 2008; Sabin et al. 2013; Fesen et al. 2020; Boumis et al. 2022; Domček et al. 2023). The optical emission of SNRs is dominated by line emission, in particular H α , and forbidden line emission from oxygen ([O III], [O I]), nitrogen ([N II]), and sulfur ([S II]). The main criterion for optical SNR identification is a line ratio of [S II]/H α ≥ 0.4 , which is useful in separating the shock emission of SNRs from photoionized gas (e.g. Fesen, Blair & Kirshner 1985).

G108.2–0.6 is a new faint and large (70 arcmin \times 54 arcmin) shell-type radio SNR discovered in the Canadian Galactic Plane Survey (CGPS) at 1420 MHz (Tian, Leahy & Foster 2007). The

SNR has an elliptical shell-type with a spectral index of $\alpha = -0.5 \pm 0.1$ ($S \sim \nu^\alpha$). The 1420 and 408 MHz observations show many bright and faint sources around the SNR: bright SNR G109.1–1.0 (southeast), faint SNR G107.5–1.5 (south), the bright H II regions Sh2–142 (southwest), Sh2–146 (east) and Sh2–148 (southeast), and the molecular cloud Sh2–152 (southeast). Tian, Leahy & Foster (2007) also presented the multi-wavelength H I, CO, infrared, X-ray, and optical investigations of G108.2–0.6. They found that H I emission associated with the SNR in the radial velocity range is from -53 to -58 km s⁻¹, and the infrared emission is close to the eastern boundary. They also reported that there is no molecular material toward the SNR, and the maps of X-ray (ROSAT) and optical (Palomar Digitized Sky Survey) show no significant emission associated with the SNR.

The distance to G108.2–0.6 was estimated to be 3.2 ± 0.6 kpc based on the H I observations (Tian, Leahy & Foster 2007). Recently, Zhao et al. (2020) determined the extinction distance of 1.02 ± 0.01 kpc from stars in the line of sight. In this work, we continue our search for optical emission from Galactic SNRs (see Bakış et al. 2023), previously discovered in the radio wavelengths, using the 1.5-m RTT150 telescope of TÜBİTAK National Observatory (TUG)¹ in Türkiye. We discovered optical filamentary and diffuse emission

★ E-mail: gunaypayli@gmail.com (GP)

† corresponding author: hicranbakis@akdeniz.edu.tr (HB)

¹ <https://tug.tubitak.gov.tr>

Table 1. Imaging observations of G108.2–0.6.

Region ID	R.A. ; Dec. (J2000)	Exposure (s)	Observation date
N region			
N1	22 51 40 ; +58 54 54	3×300	2023 July 21
		1×300	2023 Aug 14
		3×600	2023 Sep 13
N2	22 50 22 ; +58 50 12	3×300	2023 July 20
		3×600	2023 Sep 13
N3	22 52 58 ; +59 00 12	3×300	2023 Aug 15
		3×600	2023 Sep 13
S region			
S1	22 55 01 ; +58 11 58	1×300	2023 July 20
		3×300	2023 Aug 15
S2	22 53 43 ; +58 12 12	1×300	2023 July 20
		3×300	2023 Aug 15
	Filter	Wavelength (nm)	FWHM (nm)
	H α	656.3	5
	H α -cont.	644.6	13

from G108.2–0.6 through our search. We perform imaging and spectroscopic observations to investigate the optical properties of the SNR and the ambient medium. We also analyze the H I data to investigate the atomic environment of G108.2–0.6. The structure of the paper is as follows. We present observations and data reduction methods in Section 2. Analysis and results are given in Section 3. Based on these results, we infer the optical properties of the SNR and the ambient medium in Section 4 and give our conclusions in Section 5.

2 OBSERVATIONS AND DATA REDUCTION

2.1 Optical

We performed H α imaging of G108.2–0.6 with the 1.5-m RTT150 telescope. The detector is a CCD camera with 2048 × 2048 pixels, each of 13.5 μm × 13.5 μm , covering 11.1 × 11.1 arcmin² field of view (FoV). The details of imaging observations are given in Table 1. The imaging data were processed by using standard procedures with Image Reduction Analysis Facility (IRAF)², including bias and flat-field corrections.

Based on the H α imaging, the long-slit spectra of G108.2–0.6 were subsequently obtained with the TFOSC (TUG Faint Object Spectrograph and Camera) mounted at the Cassegrain ($f/7.7$) focus of the RTT150. The grism-15 was used in the spectral range between 3230 and 9120 Å including H β , [O III], H α , [N II], and [S II] emission lines with the spectral resolution of $R \sim 749$. The slit width is 2.38 arcsec, with slit length of 11.1 arcmin and the slit was oriented in the east–west direction. Table 2 lists the log of the spectroscopic observations. The data were reduced using standard procedures with IRAF, including bias subtraction, flat-field correction, wavelength, and flux calibrations. The spectrum of an Iron–Argon lamp obtained during the observations was used for wavelength calibration. For flux calibration, we used spectra taken on the same night of spectrophotometric standard star BD+28D4211 (Oke 1990).

² <https://iraf-community.github.io/>

Table 2. Spectroscopic observations of G108.2–0.6.

Slit ID	R.A. ; Dec. J(2000)	Exposure (s)	Observation date
N region			
N1a	22 51 27.5 ; +58 52 09	1×1800	2023 Jul 21
N1b	22 51 56.6 ; +58 52 51	1×1800	2023 Jul 20
N1c	22 52 08.3 ; +58 55 08	1×1800	2023 Aug 15
N2a	22 50 02.1 ; +58 53 13	1×1800	2023 Jul 21
N2b	22 50 24.1 ; +58 49 48	1×1800	2023 Jul 21
S region			
S1a	22 55 14.8 ; +58 11 11.9	1×1800	2023 Aug 14
S1b	22 55 21.2 ; +58 11 22	1×1800	2023 Aug 14
S2a	22 53 47.8 ; +58 08 50	1×1800	2023 Aug 14
S2b	22 53 41.1 ; +58 11 40	1×1800	2023 Aug 14
S2c	22 53 48.6 ; +58 08 44	1×1800	2023 Aug 15
S2d	22 53 38.4 ; +58 11 51	1×1800	2023 Aug 15

2.2 H I

We analyzed the H I line and radio continuum at 1420 MHz taken from a part of the Canadian Galactic Plane Survey (CGPS; Taylor et al. 2003), which was obtained at the Dominion Radio Astrophysical Observatory (DRAO). The angular resolution was 58'' × 80'' for the H I data and 49'' × 68'' for the radio continuum data. The typical noise fluctuation was ~ 3 K for the H I data and ~ 0.3 mJy beam⁻¹ for the radio continuum data. In Fig. 1, we show the 1420 MHz radio continuum image of G108.2–0.6 taken from the CGPS (Taylor et al. 2003).

3 ANALYSIS AND RESULTS

3.1 Optical analysis and results

3.1.1 Images

We detected optical emission from N (three locations, namely N1, N2, and N3) and S (two locations, namely S1 and S2) regions of G108.2–0.6 using the H α filter. We show the position of these regions in Fig. 1 with black boxes. The H α and continuum-subtracted H α images of the N region are given in Fig. 2. We show the H α images of the S region in Fig. 3. Due to bad weather conditions, we could not observe the S region using the H α continuum filter.

3.1.2 Spectra

Our long-slit spectra were taken on the bright optical filaments and diffuse emission in the N and S regions of the SNR (their locations are given in Table 2). In Fig. 4, we also show the slit locations on the H α images.

The long-slit spectra in the 4800–6800 Å range are presented in Figs 5 and 6, respectively. Line fluxes and their 1 σ errors were determined using the deblending function in the `splot` task in IRAF. The rms was measured on either side of the emission feature to compute errors in the measured line fluxes and then averaged. This average rms was then set as σ_0 in the `splot` error package, with `nerrsamp` set to 100 and `invgain` = 0. The line fluxes and line ratios are given in Table 3.

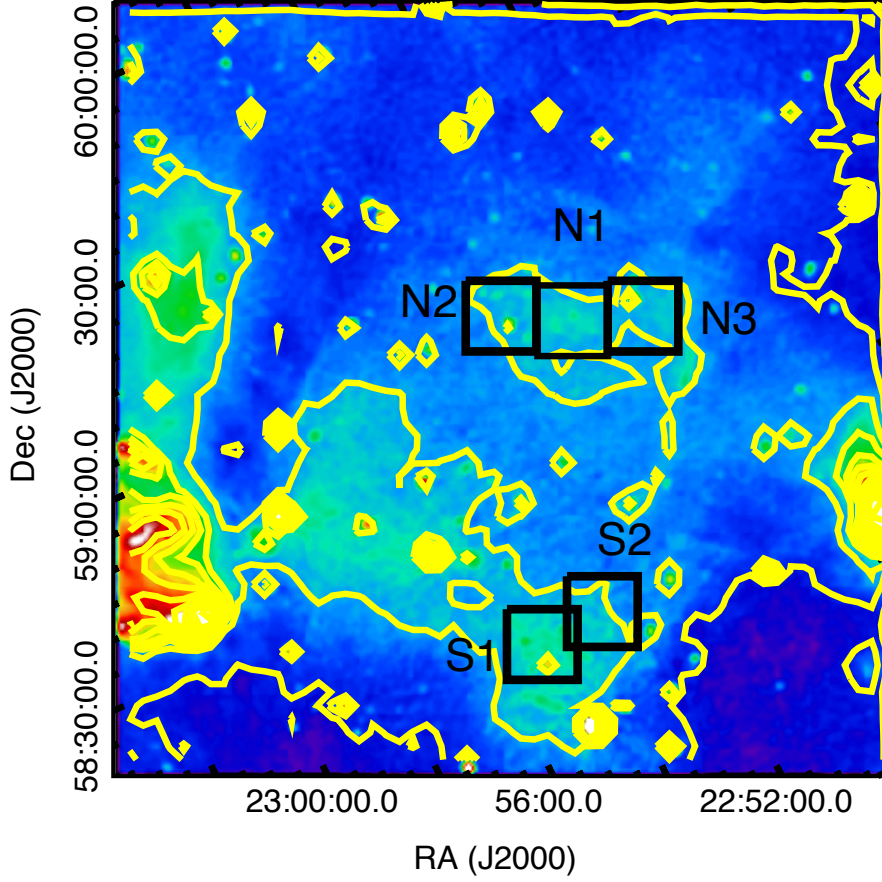


Figure 1. The 1420 MHz radio-continuum image of G108.2–0.6 taken from the CGPS (Taylor et al. 2003). The radio contour (yellow) levels range from 2.5 to 30 mJy beam⁻¹. The black boxes (11 arcmin × 11 arcmin) indicate the five regions (N1, N2, N3, S1, and S2) we observed with the RTT150 telescope.

3.2 H I analysis and results

According to Tian, Leahy & Foster (2007), the H I features in the velocity range from -58 to -53 km s⁻¹ show suggestive correlations with the radio continuum shell of SNR G108.2–0.6. On the other hand, our analysis of the same H I data found another counterpart of H I which is possibly associated with the SNR. Fig. 7(b) shows the H I integrated intensity map at the velocity range from -8.9 to 0.2 km s⁻¹, superposed on the radio shell boundary as defined by eye inspection (Fig. 7(a)). We found a cavity-like distribution of H I which shows a nice spatial correspondence with the radio shell boundary. Moreover, we newly found possible evidence for the expanding shell of H I at the same velocity range. Fig. 7(c) shows the position-velocity diagram of H I. We can see a hollowed-out distribution of H I, whose spatial extent of galactic longitude is roughly consistent with that of the SNR. The H I clouds outside of the SNR shell show a constant central velocity at ~ 3.5 km s⁻¹.

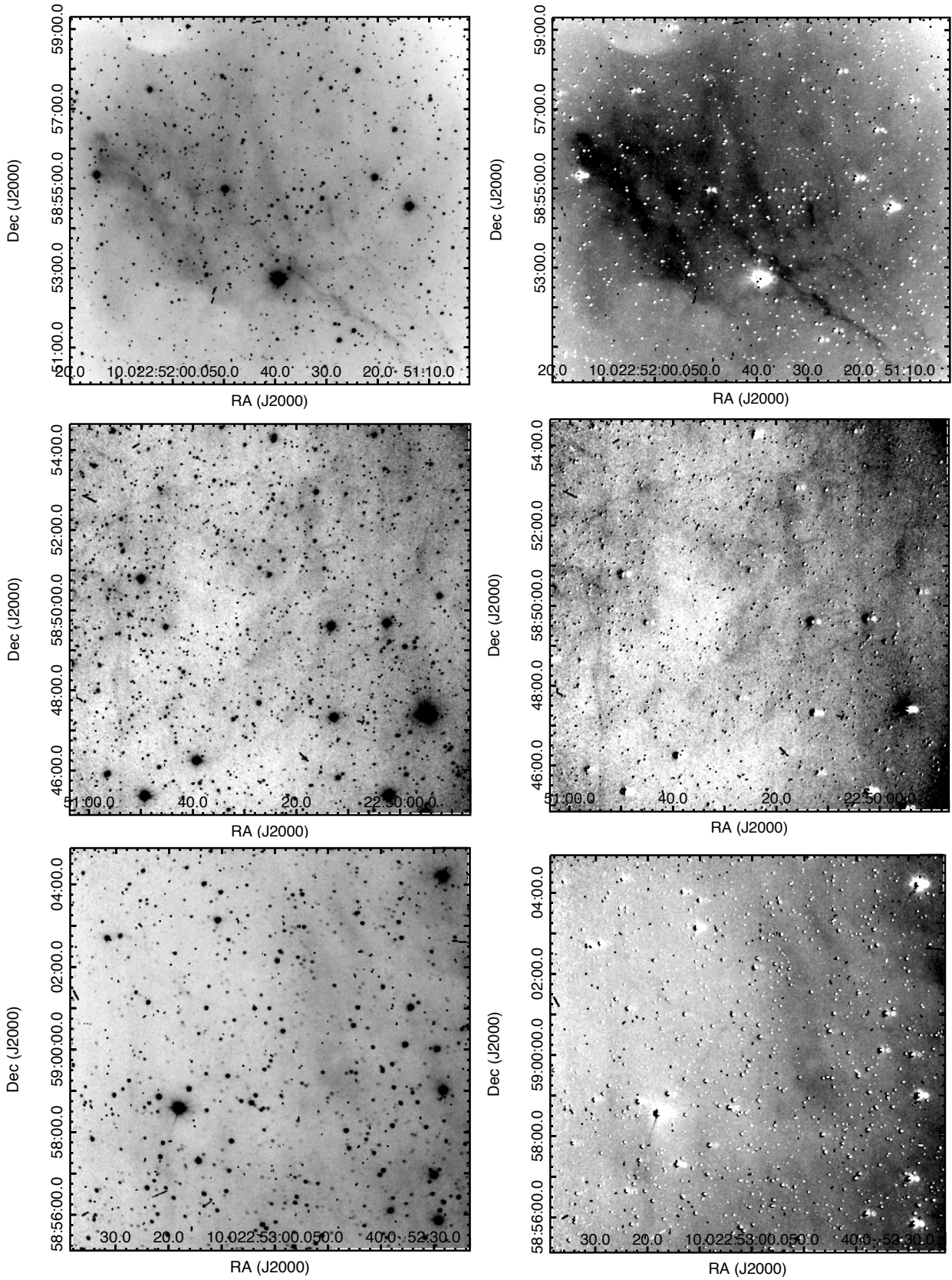


Figure 2. Top: The H α (left) and continuum-subtracted H α (right) images of N1 (top panel), N2 (medium panel) and N3 (bottom panel) regions of G108.2–0.6.

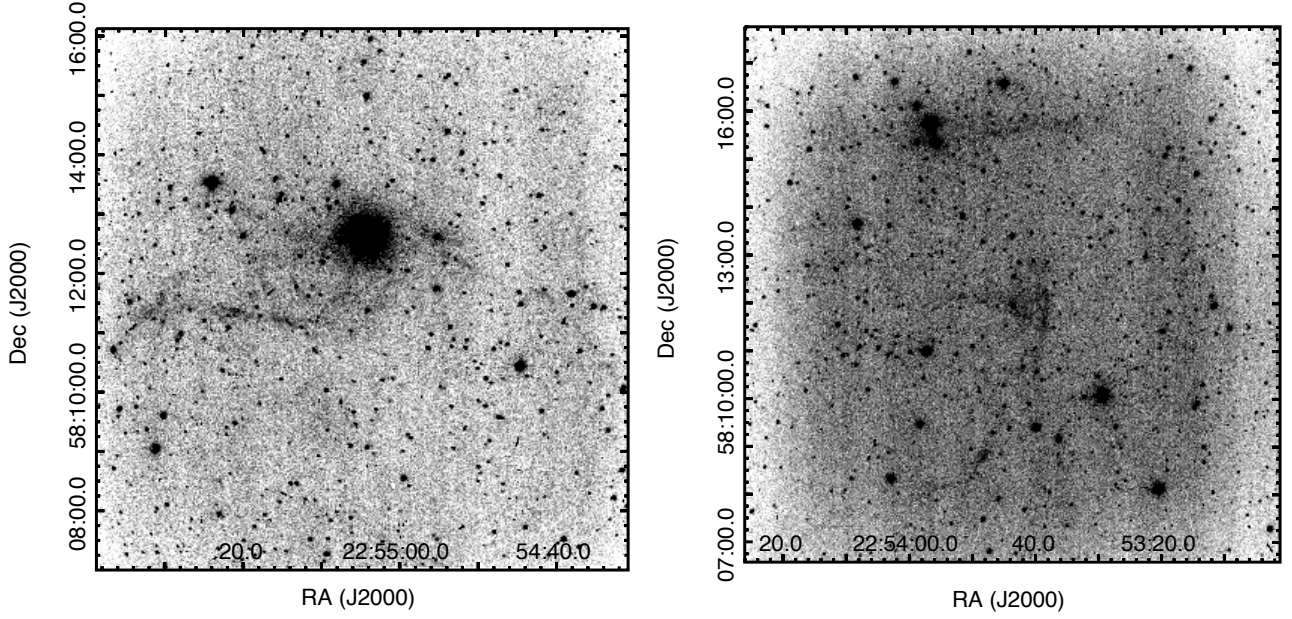


Figure 3. The $H\alpha$ image of S region (S1: left and S2: right) of G108.2–0.6.

Table 3. Line fluxes (normalised to $F(H\alpha) = 100$) with the 1σ errors. The line ratios are also presented.

	N1a	N1b	N1c	N2a	N2b	
$H\beta$ ($\lambda 4861$)	–	–	–	13 ± 2	–	
[O III] ($\lambda 4959$)	–	–	–	11 ± 2	–	
[O III] ($\lambda 5007$)	–	–	–	42 ± 2	–	
[O I] ($\lambda 6300$)	–	–	–	–	–	
[O I] ($\lambda 6363$)	–	–	–	–	–	
[N II] ($\lambda 6548$)	–	–	–	15 ± 3	–	
$H\alpha$ ($\lambda 6563$)	100 ± 6	100 ± 10	100 ± 2	100 ± 3	100 ± 2	
[N II] ($\lambda 6584$)	53 ± 8	15 ± 5	19 ± 2	34 ± 3	26 ± 2	
[S II] ($\lambda 6716$)	25 ± 9	62 ± 5	–	48 ± 3	48 ± 1	
[S II] ($\lambda 6731$)	33 ± 13	–	25 ± 2	45 ± 4	–	
$F(H\alpha)$ ($\text{erg cm}^{-2} \text{s}^{-1}$)	3.44×10^{-16}	6.20×10^{-16}	8.00×10^{-13}	5.66×10^{-17}	6.22×10^{-14}	
[S II]/ $H\alpha$	0.58 ± 0.19	0.62 ± 0.02	0.25 ± 0.02	0.93 ± 0.04	0.48 ± 0.01	
$n_e(\text{cm}^{-3})$	1800 ± 150	–	–	530 ± 40	–	
	S1a	S1b	S2a	S2b	S2c	S2d
$H\beta$ ($\lambda 4861$)	5 ± 2	–	–	–	9 ± 2	26 ± 1
[O III] ($\lambda 4959$)	6 ± 3	–	–	–	8 ± 2	–
[O III] ($\lambda 5007$)	8 ± 3	15 ± 8	–	–	20 ± 2	–
[O I] ($\lambda 6300$)	–	104 ± 3	–	23 ± 2	–	–
[O I] ($\lambda 6363$)	–	26 ± 3	–	–	–	–
[N II] ($\lambda 6548$)	–	–	–	–	–	–
$H\alpha$ ($\lambda 6563$)	100 ± 2	100 ± 8	100 ± 7	100 ± 8	100 ± 6	100 ± 2
[N II] ($\lambda 6584$)	33 ± 5	30 ± 5	30 ± 4	24 ± 4	24 ± 3	21 ± 2
[S II] ($\lambda 6716$)	23 ± 2	62 ± 5	24 ± 3	23 ± 6	28 ± 5	25 ± 1
[S II] ($\lambda 6731$)	23 ± 2	50 ± 6	17 ± 2	19 ± 5	36 ± 6	17 ± 1
$F(H\alpha)$ ($\text{erg cm}^{-2} \text{s}^{-1}$)	1.14×10^{-12}	2.32×10^{-14}	2.25×10^{-14}	1.05×10^{-14}	3.37×10^{-14}	3.38×10^{-14}
[S II]/ $H\alpha$	0.46 ± 0.03	1.12 ± 0.02	0.41 ± 0.02	0.42 ± 0.08	0.64 ± 0.07	0.42 ± 0.01
$n_e(\text{cm}^{-3})$	680 ± 20	240 ± 40	60 ± 20	280 ± 60	1640 ± 90	15 ± 10

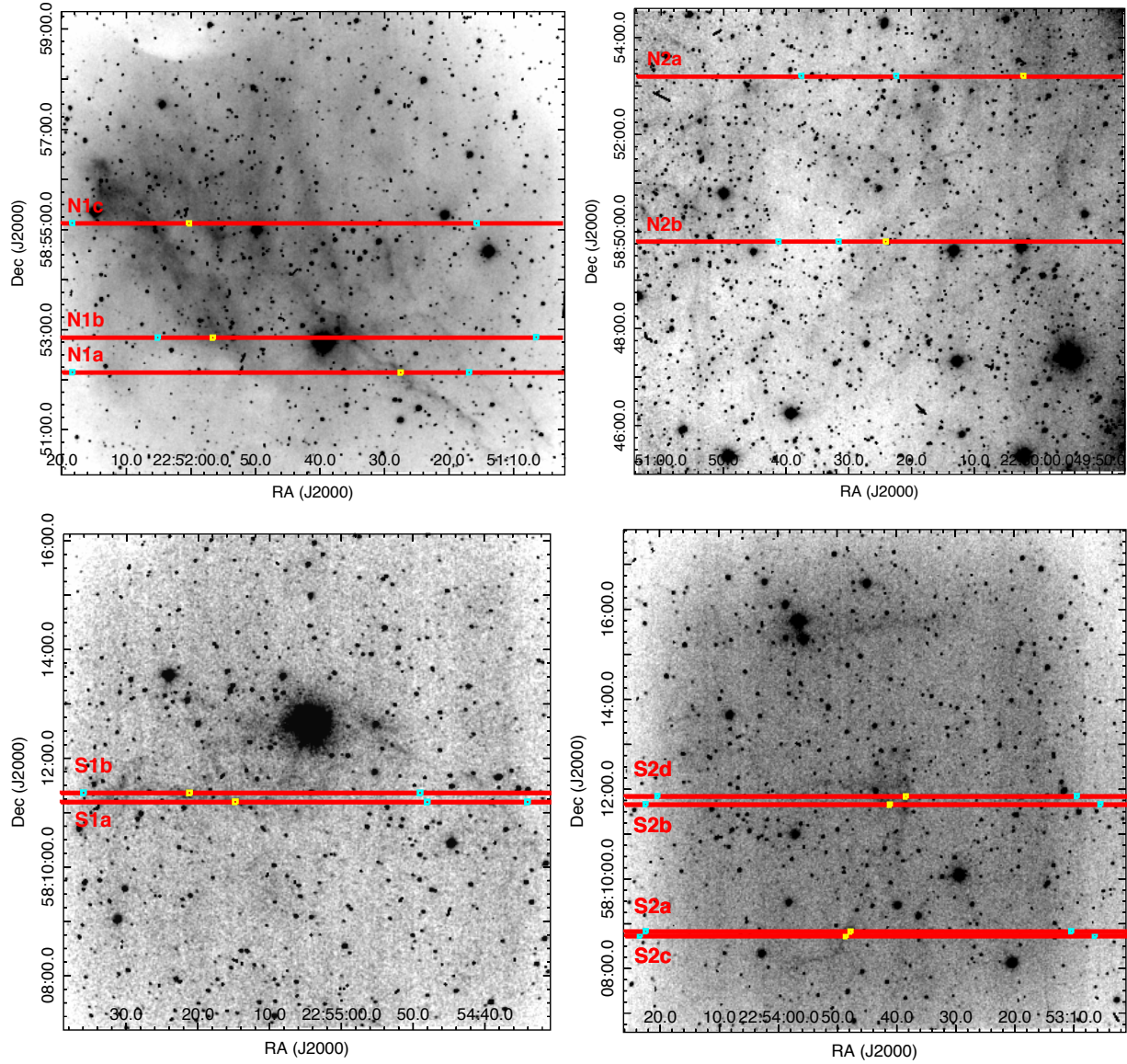


Figure 4. The location of the slits is shown on the figures. Additionally, the regions where the SNR spectra were extracted are marked with yellow boxes, and the locations for the sky subtraction along each slit are marked with cyan boxes.

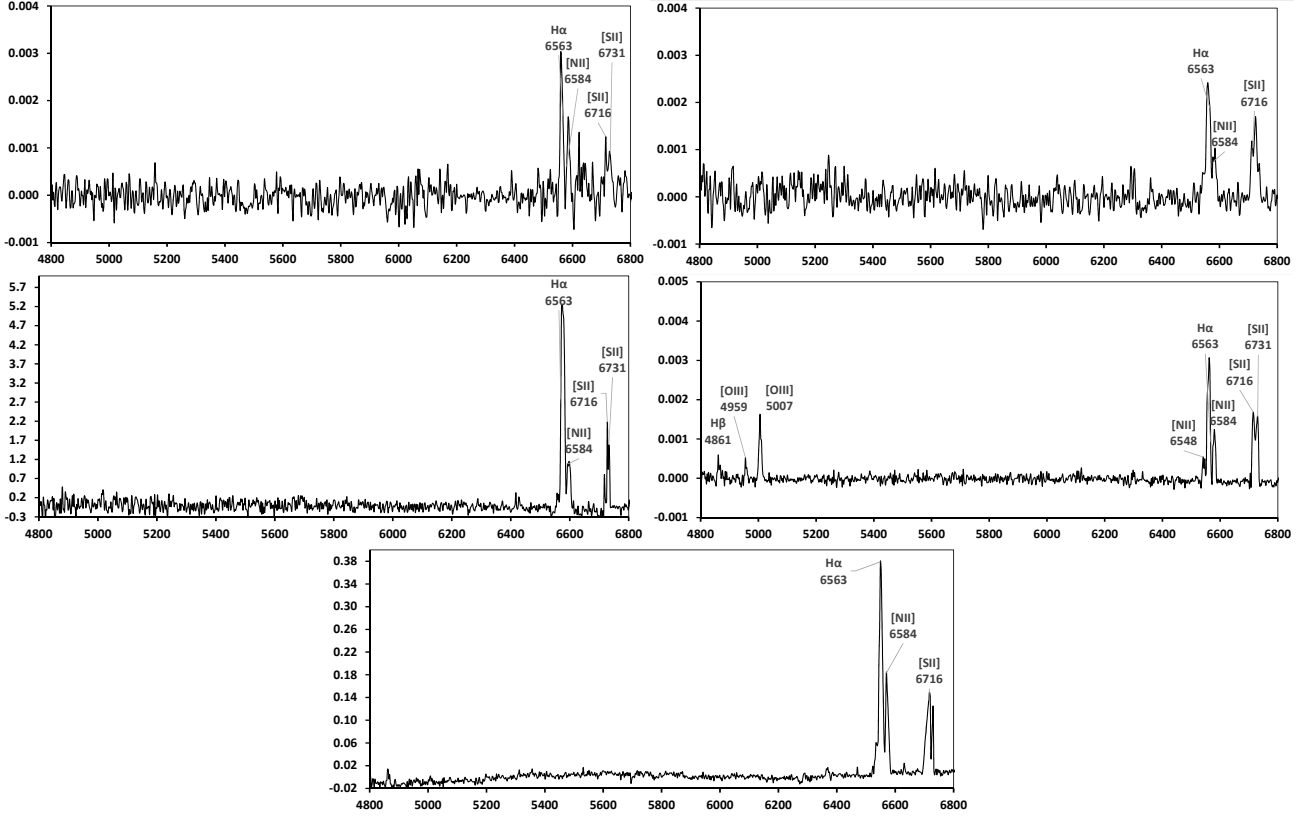


Figure 5. Long-slit spectra of five locations (N1a, N1b, N1c, N2a, and N2c) in N region of G108.2–0.6 showing the $H\beta$ λ 4861, $H\alpha$ λ 6563, $[O\ III]$ λ 4959, λ 5007, $[N\ II]$ λ 6548, λ 6584 and $[S\ II]$ λ 6716, λ 6731 lines. See Table 2 for slit locations. The y-axis shows the flux in 10^{-14} ergs cm^{-2} s^{-1} \AA^{-1} , while the x-axis shows the wavelength in Angstroms.

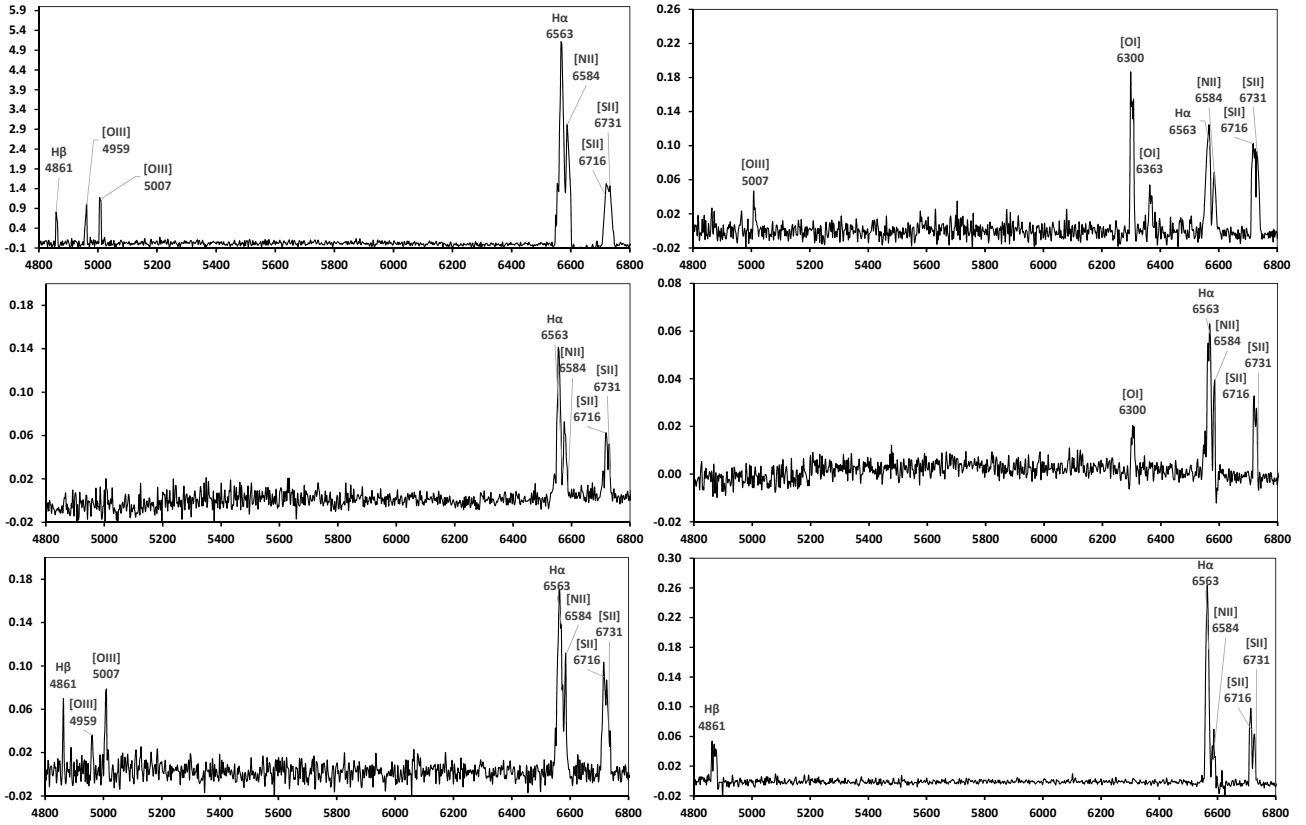


Figure 6. Long-slit spectra of six locations (S1a, S1b, S2a, S2b, S2c, and S2d) in S region of G108.2–0.6 showing the $H\beta$ λ 4861, $H\alpha$ λ 6563, $[O\ III]$ λ 4959, λ 5007, $[O\ I]$ λ 6300, λ 6363, $[N\ II]$ λ 6584 and $[S\ II]$ λ 6716, λ 6731 lines. See Table 2 for slit locations. The y-axis shows the flux in 10^{-14} ergs cm^{-2} s^{-1} \AA^{-1} , while the x-axis shows the wavelength in Angstroms.

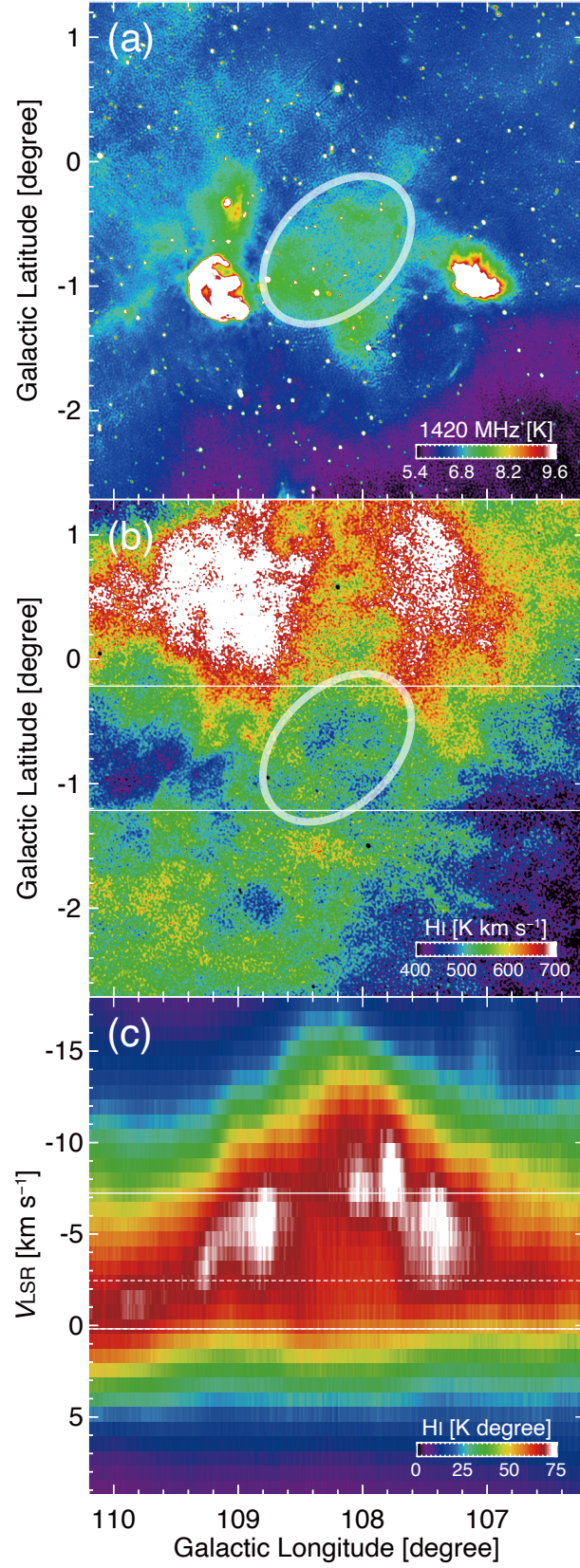


Figure 7. (a) Large-scale map of radio continuum at 1420 MHz toward G108.2–0.6 (Taylor et al. 2003). (b) Velocity-integrated intensity map of HI at $V_{\text{LSR}} = -8.9\text{--}0.2 \text{ km s}^{-1}$. The superposed circles indicate the shell boundary of the SNR. (c) Position–velocity diagram of HI. The integration range of Galactic latitude is from -1.21° to -0.21° .

4 DISCUSSION

4.1 Optical morphology

Our H α survey showed the existence of filamentary and diffuse structures, which are clearly seen and well correlate with the radio morphology as shown in Figs 1–3. The spatial correspondence of the optical emission with the radio is the strongest morphological evidence for the emission being due to the SNR.

The optical emission from G108.2–0.6 is mostly diffuse (see Figs 1–3). The detection of several filaments is consistent with the SNR emission. As can be seen in the top panel of Fig. 2, several bright, long and parallel H α filaments located in the N1 region of the SNR. The bright diffuse emission is seen in the N2 and N3 regions (see medium and bottom panels of Fig. 2). Much shorter and curved filaments are visible in the S1 and S2 regions (see Fig. 3). We note that our S1 region is close to the northeast region of SNR G107.5–1.5 (see [Kothes 2003](#); [Bakış et al. 2023](#)).

G108.2–0.6 is a large SNR, and its long and curved filament structure supports the shocks, which are expanding into a large-scale local ambient medium with varying pre-shock densities.

4.2 Optical spectral properties

The spectra exhibit [S II]/H α ratios in range 0.4–1.1, indicating emission from shock-heated gas (e.g. [Fesen, Blair & Kirshner 1985](#)), except N1c spectrum ([S II]/H α \sim 0.25) which is consistent with the photoionized gas ([Matonick & Fesen 1997](#); [Blair & Long 1997](#)).

Using the `temden` routine and assuming a temperature of 10^4 K, we calculated the electron density is ranging from 15 to 1800 cm^{-3} from the [S II] 6716/6731 ratio ([Osterbrock & Ferland 2006](#)). The high n_e values (\sim 1800 and \sim 1640 cm^{-3}) are found for the N1a and S2c slit locations can be attributed to the interaction of the SNR with a dense medium.

For the N2a, S1a, and S2c slit locations, we used the [O III] λ 5007/H β ratio and a planar shock model of [Hartigan, Raymond & Hartmann \(1987\)](#) to estimate the shock velocity V_s of \sim 80 km s^{-1} . Other slit locations lack [O III] emission, indicating shock velocities less than about \sim 70 km s^{-1} .

We then derived the pre-shock cloud density (n_c) to be \sim 18–57 cm^{-3} taking the relation

$$n_{[\text{S II}]} = 45 n_c \times (V/100 \text{ km s}^{-1})^2 \text{ cm}^{-3} \quad (1)$$

from [Fesen & Kirshner \(1980\)](#), where $n_{[\text{S II}]}$ is the electron density calculated from the sulfur line ratio.

We detected H β emission in the N2a, S1a, S2c, and S2d locations and therefore can estimate the extinction in these directions. We found extinction $E(B-V)$ value of \sim 0.22–1.65 using the H α /H β ratio and assuming that $E(B-V) = 0.664c$, where c is a logarithmic extinction (see [Kaler 1976](#); [Aller 1984](#)). We finally estimated the column density N_{H} of \sim (1.2–8.9) $\times 10^{21} \text{ cm}^{-2}$ using the relation $N_{\text{H}} = 5.4 \times 10^{21} \times E(B-V)$ ([Predehl & Schmitt 1995](#)). The extinction and column density values show significant variation across the observed regions.

Overall, our optical spectral investigation shows that G108.2–0.6 is expanding into dense and complex areas, which agrees well with the conclusion reported in [Tian, Leahy & Foster \(2007\)](#).

4.3 Atomic environment

Our analysis found alternative counterparts of H I clouds (V_{LSR} : -8.9 – 0.2 km s^{-1}) possibly associated with the SNR. The cavity-

like structures of H I shown in Figs 7(b) and 7(c) are likely an expanding H I shell which was generally formed by strong stellar winds from the progenitor and/or supernova shocks (e.g., [Koo et al. 1990](#); [Koo & Heiles 1991](#)). When we adopt the systemic velocity of the H I clouds to be \sim 3.5 km s^{-1} , the expanding velocity of the H I cloud gives \sim 5 km s^{-1} , which is roughly consistent with other Galactic/Magellanic SNRs (e.g., [Sano et al. 2017, 2019](#); [Kuriki et al. 2018](#)). The shock front of the supernova is now impacting on the inner wall of the H I expansion shell.

4.4 Distance and Age

If the H I cloud at $V_{\text{LSR}} = -8.9$ – 0.2 km s^{-1} is physically associated with SNR G108.2–0.6, we may reconsider the distance to the SNR. By adapting the Galactic rotation model with the IAU-recommended values ($R_0 = 8.5 \text{ kpc}$, $\Theta_0 = 220 \text{ km s}^{-1}$; [Kerr & Lynden-Bell 1986](#); [Brand & Blitz 1993](#)), we obtain a kinematic distance of the H I cloud and SNR G108.2–0.6 as \sim 0.8 kpc. This value is roughly consistent with the extinction distance ([Zhao et al. 2020](#)). At the distance, we derived the diameter of SNR G108.2–0.6 to be $16.3 \text{ pc} \times 12.6 \text{ pc}$. By assuming the Sedov–Taylor model ([Sedov 1959](#)), the dynamical age of SNR G108.2–0.6 can be estimated to be \sim 70 \pm 10 kyr.

5 CONCLUSIONS

In this work, we report the first detection of optical emission from G108.2–0.6 based on both H α imaging and spectroscopic observations. The filamentary structure of G108.2–0.6 is consistent with its SNR nature. Our spectra exhibit the H β λ 4861, [O III] λ 4959, λ 5007, [O I] λ 6300, λ 6363, H α λ 6563, [N II] λ 6584 and [S II] λ 6716, λ 6731 lines. The [O I] λ 6300, λ 6363 lines detected in the S region also support the indicator of the presence of shocks. The [S II]/H α ratios suggest that the shock-excited gas for G108.2–0.6. We found the electron density ranging from 15 to 1800 cm^{-3} using [S II] 6716/6731. The spectra show a relatively low shock velocity of $V_s \sim$ 80 km s^{-1} with the pre-shock cloud density of $n_c \sim$ 18–57 cm^{-3} . We also estimated the kinematic distance to the SNR of \sim 0.8 kpc and the dynamical age as \sim 70 \pm 10 kyr using the archival H I data. Further observations with different frequencies are needed to better understand the nature of this SNR.

ACKNOWLEDGEMENTS

We thank TÜBİTAK National Observatory for partial support in using RTT150 with project number 1562. HS was supported by JSPS KAKENHI grant No. 21H01136. The Canadian Galactic Plane Survey (CGPS) is a Canadian project with international partners. The Dominion Radio Astrophysical Observatory is operated as a national facility by the National Research Council of Canada. The CGPS is supported by a grant from the Natural Sciences and Engineering Research Council of Canada. We also thank the referee for valuable comments and suggestions that helped to improve the paper.

DATA AVAILABILITY

The optical data from the RTT150 telescope will be shared on reasonable request to the corresponding author.

REFERENCES

- Aller L. H., 1984, *Physics of thermal gaseous nebulae* (D. Reidel Publishing Company)
- Bakış H., Bulut G., Bakış V., Sano H., Sezer A., 2023, *MNRAS*, **521**, 1099
- Blair W. P., Long K. S., 1997, *ApJS*, **108**, 261
- Boumis P. et al., 2022, *MNRAS*, **512**, 1658
- Brand J., Blitz L., 1993, *A&A*, **275**, 67
- Domček V. et al. 2023, *MNRAS*, **526**, 1112
- Dubner G., Giacani E., 2015, *A&ARv*, **23**, 3
- Fesen R. A., Kirshner R. P., 1980, *ApJ*, **242**, 1023
- Fesen R. A., Blair W. P., Kirshner R. P., 1985, *ApJ*, **292**, 29
- Fesen R. A. et al. 2020, *MNRAS*, **498**, 5194
- Green D. A., 2019, *J. Astrophys. Astron.*, **40**, 36
- Hartigan P., Raymond J. C., Hartmann L. W., 1987, *ApJ*, **316**, 323
- Kaler J. B., 1976, *ApJS*, **31**, 517
- Kerr F.J., Lynden-Bell D., 1986, *MNRAS*, **221**, 1023
- Koo B.-C., Heiles C. 1991, *ApJ*, **382**, 204
- Koo B.-C., Reach W. T., Heiles C., Fesen R. A., Shull J. M., 1990, *ApJ*, **364**, 178
- Kothes R., 2003, *A&A*, **408**, 187
- Kuriki M. et al., 2018, *ApJ*, **864**, 161
- Matonick D. M., Fesen R. A., 1997, *ApJS*, **112**, 49
- Oke J. B., 1990, *AJ*, **99**, 1621
- Osterbrock D. E., Ferland G. J., 2006, *Astrophysics of Gaseous Nebulae and Active Galactic Nuclei* (Mill Valley, CA: Univ. Science Books)
- Predehl P., Schmitt J. H. M. M., 1995, *A&A*, **293**, 889
- Sabin L. et al., 2013, *MNRAS*, **431**, 279
- Sano H. et al., 2017, *ApJ*, **843**, 61
- Sano H. et al., 2019, *ApJ*, **881**, 85
- Sedov L. I., 1959, *Similarity and Dimensional Methods in Mechanics*. Academic Press, New York, NY
- Stupar M., Parker Q. A., Filipovic M. D., 2008, *MNRAS*, **390**, 1037
- Taylor A. R. et al., 2003, *AJ*, **125**, 3145
- Tian W. W., Leahy D. A., Foster T. J., 2007, *A&A*, **465**, 907
- Vink J., 2020, *Physics and Evolution of Supernova Remnants*. Astronomy and Astrophysics Library, Springer International Publishing, Cham, doi:10.1007/978-3-030-55231-2, <http://link.springer.com/10.1007/978-3-030-55231-2>
- Zhao H., Jiang B., Li J., Chen B., Yu B., Wang Y., 2020, *ApJ*, **891**, 137

This paper has been typeset from a $\text{\TeX}/\text{\LaTeX}$ file prepared by the author.